Materials & Design 264 (2026) 115812

Contents lists available at ScienceDirect

Materials & Design

journal homepage: www.elsevier.com/locate/matdes

Rapid low-temperature, vacuum-free metallization via melted metal spray for electronic and photovoltaic devices

Samuel Porcar-Garcia [a,*], Olfa Selmi [b], Abderrahim Lahlahi [a], Santiago Toca [a], Antoni Merin [c], Xavier Alcobe [c], Sofia Masi [b], Rosario Vidal [b], Iván Mora-Seró [b], Jaime González-Cuadra [a,d], Juan Bautista Carda [a]

[a] Departamento de Química Inorgánica y Orgánica, Universitat Jaume I (UJI), Av. Vicent Sos Baynat s/n, 12071 Castelló de la Plana, Spain
[b] Institute of Advanced Materials (INAM), Universidad Jaume I, Av. Sos Baynat s/n, 12071 Castelló, Spain
[c] Centres Científics i Tecnològics de la Universitat de Barcelona (CCiTUB), Lluís Solé i Sabarís 1-3, 08028 Barcelona, Spain
[d] Dept. of Materials and Ceramic Engineering/CICECO-Aveiro Institute of Materials, University of Aveiro, Campus Universitario de Santiago, Aveiro 3810-193, Portugal

ARTICLE INFO

Keywords:
Low-costmetallization
Low-temperature metallization
Photovoltaic solar cell
Back contact
Melted metal spray
Vacuum-free deposition
Life cycle assessment

ABSTRACT

This work introduces the **Melted Metal Spray (MMS)** process, a simple and highly accessible rapid prototyping metallization technique that enables **metal deposition under ambient conditions** without the need for vacuum systems or elevated temperatures. The MMS method achieves uniform metallic layers in **less than 10 s** with a minimal thermal load on the substrate (temperature rise < 3 °C) making it highly suitable **for thermally sensitive materials**. Compared with conventional metallization approaches that rely on high-vacuum or high-temperature environments, MMS offers an **environmentally benign, cost-effective and scalable alternative** using simple equipment and air operation. The resulting metallic films exhibit **electrical performance comparable to thermally evaporated silver**, achieving a specific contact resistivity of **0.43 ± 0.11 mΩ·cm^2** at the metal/ fluorine-doped tin oxide (FTO) interface for a ~100 µm thick layer deposited electrodes. The method's **compatibility with a wide range of substrates**, including polymeric supports, enables the fabrication of conductive circuits that maintain functionality under mechanical deformation highlighting its potential for **flexible and wearable electronics**. Moreover, the successful integration of MMS contacts into **perovskite photovoltaic devices** demonstrates its feasibility for emerging optoelectronic applications. Overall, MMS represents a **promising low power requirements, low-cost, low-temperature, and vacuum-free metallization strategy** for next-generation electronic and photovoltaic systems.

1. Introduction

The global shift toward renewable energy sources has positioned electronic and optoelectronic devices such as photovoltaic (PV) technologies as key players in sustainable energy strategies [1–4]. Among them, perovskite solar cells (PSCs) have emerged as highly promising due to their combination of high efficiency and low manufacturing costs [5–7]. Although most efforts to improve these technologies focus on the research of absorber materials, photovoltaic devices are composed of other semiconductor or metallic layers that also play a crucial role in achieving high efficiency [8]. These include hole-transport layers (HTL), electron-transport layers (ETL), and both the front (FC) and rear or back electrical contacts (BC) necessary for ensuring efficient current flow. While these other layers often receive less attention, they are equally important for achieving high device efficiency and reducing the time and cost of production, whether at the laboratory scale or on a more commercial level [9,10].

In recent years, a series of organic hole transport layers (HTL), such as poly(triarylamine) (PTAA) or poly(3,4-ethylenedioxythiophene) (PDOT), have emerged, enabling the formation of these layers quickly and at lower temperatures, thus speeding up the synthesis of devices (especially at the laboratory scale) [11]. Furthermore, the use of these layers allows for the reduction of the necessary equipment to form HTL as they no longer depend on high-vacuum equipment reducing also the costs [12]. This enables work on cells that are more sensitive to thermal stress in a more agile and cost-effective manner. However, despite these advances improves the fabrication process, a bottleneck remains in the device fabrication. The metallization of the device to form a back

* Corresponding author.
E-mail address: saporcar@uji.es (S. Porcar-Garcia).

https://doi.org/10.1016/j.matdes.2026.115812
Received 13 January 2026; Received in revised form 4 March 2026; Accepted 5 March 2026
Available online 9 March 2026
0264-1275/

contact or the creation of the front contact (e.g., fluorine-doped tin oxide (FTO), aluminum-doped zinc oxide (AZO), or indium tin oxide (ITO)) with the current deposition methods, either for the fabrication of a solar cell or simply for the generation of an electrical contact in most electronic devices, requires choosing between working in high vacuum, which significantly increases the time and cost of the operation, or working at high temperatures under air, which can thermally degrade other layers of the device also making poorer quality films [13–15].

High-vacuum methods enable the controlled deposition of high-purity metallic films with good adhesion and uniformity [16]. However, they also come with significant drawbacks: high capital and operational costs, time-consuming procedures, and the need for sophisticated vacuum equipment and inert conditions. Such requirements present a major technical and economic barrier, particularly for decentralized or resource-limited research environments [17,18].

To reduce dependency on vacuum-based systems, a variety of alternative metallization strategies have been developed [19]. Among them, solution-based techniques such as inkjet printing, spin coating, spray coating, and chemical plating offer the advantage of ambient-condition processing and lower equipment costs [20,21]. Nevertheless, these methods often suffer from limitations that make them less attractive. For instance, ink-based techniques typically require post-deposition thermal annealing to remove solvents and sinter nanoparticles into a conductive film, conditions that may be incompatible with temperature-sensitive materials, especially under air like lead-halide perovskites and making the process slower. Moreover, achieving uniform coverage and low specific contact resistivity on complex or textured surfaces remains a challenge [22]. Chemical plating and electrodeposition, while suitable for low-temperature processing, involve complex solution chemistries and are highly sensitive to substrate conductivity and surface cleanliness [23]. In many cases, these processes can lead to non-uniform films or damage to the underlying layers [24].

Aiming to address the limitations of current metallization techniques, we introduce Melted Metal Spray (MMS), a novel hybrid method that combines elements of spray coating and thermal spraying while overcoming their main drawbacks (Fig. 1). MMS involves spraying a low-melting-point metallic alloy in its molten or semi-molten state directly onto the device surface, forming a conductive contact layer in just a few seconds in an easy manner and using cost-effective, accessible equipment. By carefully tuning the alloy composition, droplet size, and spray parameters, the room temperature substrate temperature remains below 30 °C during deposition, making the method highly compatible with thermally sensitive materials. Unlike conventional spray techniques, MMS uses no solvents, requires no post-deposition treatment, and is performed entirely in ambient air, without vacuum or inert atmospheres. The moderate kinetic energy of the molten droplets reduces mechanical stress and allows for good adhesion while maintaining compatibility with delicate underlying layers.

In this context, MMS differs fundamentally from other vacuum-free metallization approaches frequently cited in the literature. Cold spray processes rely on the acceleration of solid metal particles to very high velocities, where film formation is governed by severe plastic deformation upon impact. While effective for thick and robust coatings, such high kinetic energies can induce surface damage and are generally unsuitable for microelectronic devices or fragile thin-film stacks [25]. Aerosol jet printing and related ink-based techniques, in contrast, atomize solvent-borne nanoparticle suspensions, requiring post-deposition drying and sintering to achieve electrical percolation. These steps can introduce thermal stress, residual organics, and compatibility issues with temperature-sensitive layers [26].

In recent years, some free solvent aerosol-based approaches for metal deposition under ambient conditions have also been explored using room-temperature liquid metals such as eutectic Ga–In alloys [27]. These methods enable the patterning of conductive traces through the spraying or printing of liquid metal droplets and have been successfully applied to stretchable and soft electronics. It main drawback is that the deposited material remains liquid after deposition, and electrical conduction relies on percolative or fluidic mechanisms enabled by the presence of a surface oxide layer. As a result of the liquid state, the resulting metallic layers are mechanically compliant but are soft and can be susceptible to smearing, often requiring encapsulation or secondary protective layers to ensure long-term stability [28].

By comparison, MMS deposits a fully molten or semi-molten low-melting-point alloy that rapidly solidifies upon impact, producing a continuous metallic layer through wetting and solidification. This approach is inherently constrained by the availability of alloy systems compatible with low melting temperatures, as discussed later in the manuscript, but avoids the use of solvents, nanoparticle necking or sintering, and vacuum processing. As a result, MMS constitutes a solvent-free molten-alloy transfer approach that is distinct from both particle-impact and ink-percolation-based metallization methods, while retaining operational simplicity and a very low thermal budget.

Beyond serving as an alternative deposition technique, MMS

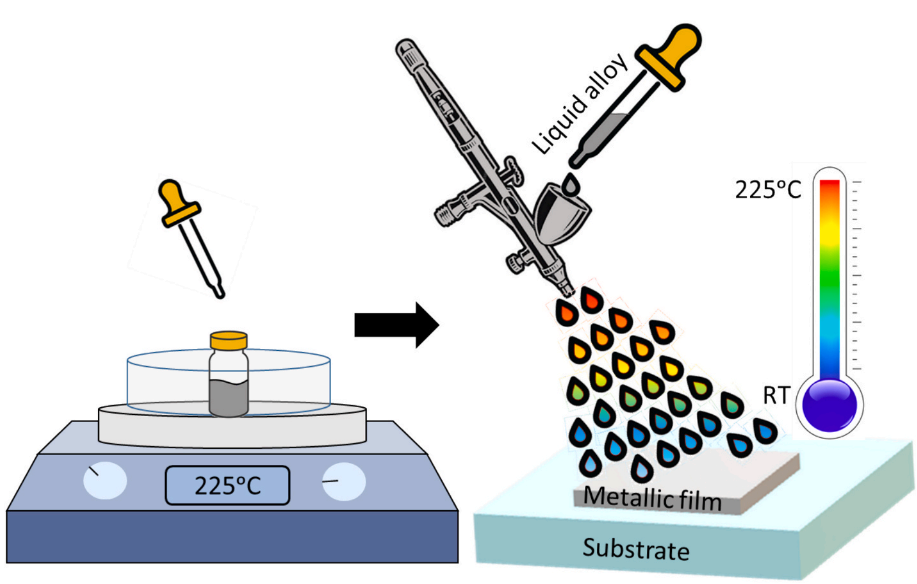

Fig. 1. Schematic of the metallization process.

introduces a different paradigm for metallization in electronic device fabrication. By decoupling metal contact formation from vacuum infrastructure, solvent processing, or high thermal budgets, MMS enables late-stage, rapid contact integration compatible with thermally fragile multilayer stacks. This shift has direct implications for device design, particularly for perovskite and flexible electronics, where metallization often dictates processing constraints and infrastructure requirements. Rather than incrementally optimizing existing vacuum-based workflows, MMS redefines metallization as a low-energy, ambient, and infrastructure-light step, potentially facilitating decentralized prototyping and accelerated laboratory-scale device development.

In this study, we explore the viability of MMS as a metallization route for electronic devices, focusing on its implementation in perovskite solar cells and conductive circuits to demonstrate the versatility of the method. Two low-melting-point metal alloy compositions were developed: an indium–tin–zinc alloy (ITZ) and an indium–tin–gallium alloy (ITG), both designed to melt below 110 °C to ensure compatibility with the MMS methodology. These alloys were evaluated in terms of their thermal behavior, film morphology, and electrical contact performance, and their results were benchmarked against thermally evaporated silver and printed silver ink on identical device stacks. Finally, proof-of-concept integration into fully functional perovskite devices and flexible conductive circuits is presented, positioning MMS as a practical and accessible alternative to conventional vacuum-based metallization strategies.

2. Methods

2.1. Materials and reagents

All chemicals used for the device fabrication were of analytical grade and used directly without further purification. The chemicals used were Indium (99.99%), tin (99.5%, Sigma Aldrich), gallium (99.99%) and zinc (99.95%), silicone oil for heating (Labkem), clorhidric acid (Fuming 37%, Supelco), ethanol absolute, Isopropanol (99.5%, Sigma Aldrich), FTO coated glass (7 Ω/sq, Sigma Aldrich). Formamidinium bromide (FABr, 98% purity, sourced from GreatCell Solar), lead bromide ($PbBr_2$, >98% purity, obtained from TCI), N,N-dimethylformamide (DMF, anhydrous, 99.9% purity), dimethyl sulfoxide (DMSO, anhydrous, 99.9% purity), chlorobenzene (CB, anhydrous, 99.8% purity), Poly(3,4-ethylenedioxythiophene):poly(styrenesulfonate) (PEDOT: PSS) Al 4083 aqueous solution was procured from Heraeus. Indium tin oxide (ITO) substrates (Pilkington TEC-15, a sheet resistance of approximately 15 Ω/sq) were used as the base material for fabricating perovskite solar cells (PSCs).

2.2. Films deposition methodology

Two different compositions of metallic alloys were prepared prior to the deposition of the metallic film. For the preparation, a vial with the metallic precursors in the nominal atomic ratios listed in Table 1 was placed in a silica gel bath at 225 °C and was stirred with a stirring wand for 5 min until the melted metalls became a homogeneous alloy. The compositions of both alloys Indium, tin and zinc (ITZ) and indium tin and Gallium (ITG) is shown in Table 1.

For the deposition of the metallic films, a Timbertech airbrush connected to a Timbertech ABPS compressor was used. The airbrush was modified with a 0.5 mm nozzle, and the needle was removed to allow the liquid to flow due to the high viscosity of the metal alloys. The gas used to propel the liquid was air at a pressure of 2 atm and the shooting distance was 10 cm. As described in Fig. 1 previous to the deposition the alloys were heated at 225 °C in a silica gel bath and the aerograph was warmed up to placing it on the hot plate 2 min before the shot. The target substrate was covered with a mask with the desired pattern. Finally, the aerograph was taken with heat-protective gloves and 4 drops of the solution were dropped on it, after that, a ~125 μm thick film was shot on the substrate being deposited. The time of deposition can vary depending on the dimensions of the sample and the amount of samples deposited at the same time, but for a 2 × 2 cm target the deposition time is approximately 5 s.

Deposited metal placed on masks near the deposited electrodes, can be easily recycled, making the deposition process cheaper and generating less environmental impact. For this propose, the metallic waste placed on the mask or near of the deposited samples can be recovered (see **Fig. S1**). For it, the surfaces of the masks and the surroundings were scratched with a plastic spatula and the recovered metal fragments were placed in a vial. To eliminate the metallic oxides generated during the deposition, enough HCl 10% to cover all the metallic powder was placed in the vial, and the mixture was heated to the alloy melting point. When all the metal particles came together in a single liquid shining metallic drop, the vial was cooled and the HCl was eliminated. The vial with the solid metallic drop was rinsed two times with ethanol and isopropanol, after that, the drop was placed in the original precursor metallic alloy vial.

Table 1
Atomic composition for the ITZ and ITG.

Alloy	Indium at%	Tin at%	Zinc at%	Gallium at%
ITZ	52.3	44.6	3.2	–
ITG	48	37	–	15

2.3. Devices fabrication

For the fabrication of the perovskite solar cells the ITO-coated glass substrates were chemically etched using zinc powder and 6 M HCl to obtain the desired ITO pattern. The etched substrates underwent sequential cleaning in an ultrasonic bath for 15 min each, using soap water, acetone, ethanol and isopropanol, respectively. After cleaning, the substrates were dried with nitrogen (N_2) flow and exposed to UV-Ozone treatment for 20 min.

The PEDOT:PSS as a hole transport layer was spin-coated onto the ITO surface at 5000 rpm for 40 s with an acceleration of 2000 rpm/s and annealed at 130 °C for 20 min under ambient conditions. Then, the substrates were transferred to a nitrogen-filled glovebox for the deposition of the $FAPbBr_3$ perovskite layer. The $FAPbBr_3$ was prepared by dissolving 62.5 mg of FABr (1 mmol) + 196.4 mg PbBr2 (1.07 mmol) in 750 μl DMF + 250 μl DMSO and spin coated at 3000 rpm for 30 s. 300 μl of toluene as antisolvent was dropped at 10 s and annealed at 90 °C for 10 min.

After the perovskite deposition, a PCBM solution (28 mg/mL in chlorobenzene) was prepared and spin-coated onto the perovskite films at 2000 rpm for 30 s followed by annealing at 70 °C for 10 min. Subsequently, a BCP solution (0.5 mg/mL in isopropanol) was spin-coated at 6000 rpm for 30 s and annealed at 70 °C for 5 min. Finally, to complete the devices different strategies were used. For the control dispositive, 100 nm of silver was thermally evaporated onto the layers as the metal contact, also two more devices were made using the metallic compositions previously mentioned using the MMS technique.

In the case of the conductive circuits, a mask was placed on the paper or nitrile-based elastomers and the metallic alloys were sprayed. The deposition of the metallic circuit directly onto the glove is shown in **Supporting** Video 1.

2.4. Measurements and characterization

The temperature of the substrate during the deposition of the metallic film was measured using an infrared thermometer ST60 Proplus with a measurement time of 0.5 s and a repeatability of ±1 °C. For XRD analysis an Anton Paar XRDynamic 500 multipurpose powder diffractometer equipped with an Anton Paar CHC plus + Cryo and Humidity

Chamber was used. 2θ/θ 1D scans, 5–80° 2θ with a step size of 0.02° 2θ and with a measuring time of 50.173 s per step (total scan duration 13 min) were made. Scanning Electron Microscopy (SEM), model JEOL 7001F, equipped with energy dispersive X-ray analysis (EDX), was used to investigate the morphology and elemental composition of the metallic alloys. Transmission line model or Transfer Length Method (TLM) measurements were made using a Keithley 2400 SourceMeter to calculate the specific contact resistivity between our metallic layers and an FTO layer. Differential Scanning Calorimetry (DSC) was performed using a Mettler Toledo DSC2 heat flow calorimeter. The system operates with a 400 W power supply and is equipped with an FRS6 ceramic sensor, offering a measurement resolution of up to 0.04 μW. The solar cells were optoelectronically characterized through I-V curves measured with a Solar Simulator model SunLite 11002 Class AAB, providing uniform AM 1.5 illumination over a 50 × 50 mm area at a temperature of 298 K. All solar cell parameters and efficiencies reported in this study refer to the active area (0.25 cm^2) of the devices. The roughness was evaluated over 636.61 × 477.25 μm^2 area using a PLμ 2300 optic profilometer.

To evaluate the minimum printable resolution of the method, a test pattern with line/space widths of 1000, 500, 250, 150, and 100 μm was fabricated, and after deposition the resistance of each line was measured using a four-point probe configuration with a Keithley 2400 SourceMeter. Mechanical reliability was assessed through bending and stretching tests. For bending, 1000 cycles of an S-bend test were performed over a mandrel with a 5 mm radius, recording the resistance every 100 cycles. For stretching, resistance was measured at 5, 10, 15, and 20% strain, and cyclic durability was evaluated by monitoring the resistance after 1, 10, 100, 500, and 1000 stretching cycles at 20% strain. All measurements were performed on three independently prepared samples for each condition, and the reported values correspond to the average results, with deviations within the experimental uncertainty.

3. Results

3.1. Deposition temperature profile

The impact of the variation on the surface temperature of the substrate was measured using a thermic gun ST60 Proplus. Some measurements were tried with thermocouples but because of the low impact of the deposition on the temperature of the substrate and the speed of the process was not viable to measure by that manner. To measure it, the thermal gun was aimed at an FTO-coated glass substrate at 25 °C. After placing a mask with the desired deposition pattern on the substrate, a metallic layer was deposited, and the temperature was recorded for 30 s. In Fig. 2a we can observe a warming of 5 s until approximately 27.4 °C that was the time that takes to the film to be deposited on the substrate, followed by the free cooling of the sample in air.

3.2. Structural and thermal characterization

In the Fig. 2b and c it is shown the XRD of the ITZ and ITG alloys at different temperatures. Fig. 2b shows the XRDs of the sample ITZ between 0 and 120 °C. In it, two main structural types (phases) were identified: (γ) (tin rich) (In,Sn), hexagonal *P6/mmm* (PDF#04-003-3254) and (β)(indium rich) (In,Sn) tetragonal *I4/mmm* (PDF#04-002-9972). Moreover, Zn hexagonal *P63/mmc* (PDF#04-008-6027) was identified as a minor, third, crystalline phase. All the phases are observable until 120 °C, when the peaks disappear due to the melting of the alloy.

Before measuring the ITG sample, it was cooled below −50 °C by resting on dry ice for 1 h. Then, the sample was rapidly transferred to the CHC+ equipment chamber, where measurements were conducted to determine the melting temperatures of the metal. Fig. 2c depicts the obtained sum diffractograms at temperatures between 0 and 80 °C. Under 20 °C three main phases can be observed, a Ga orthorhombic

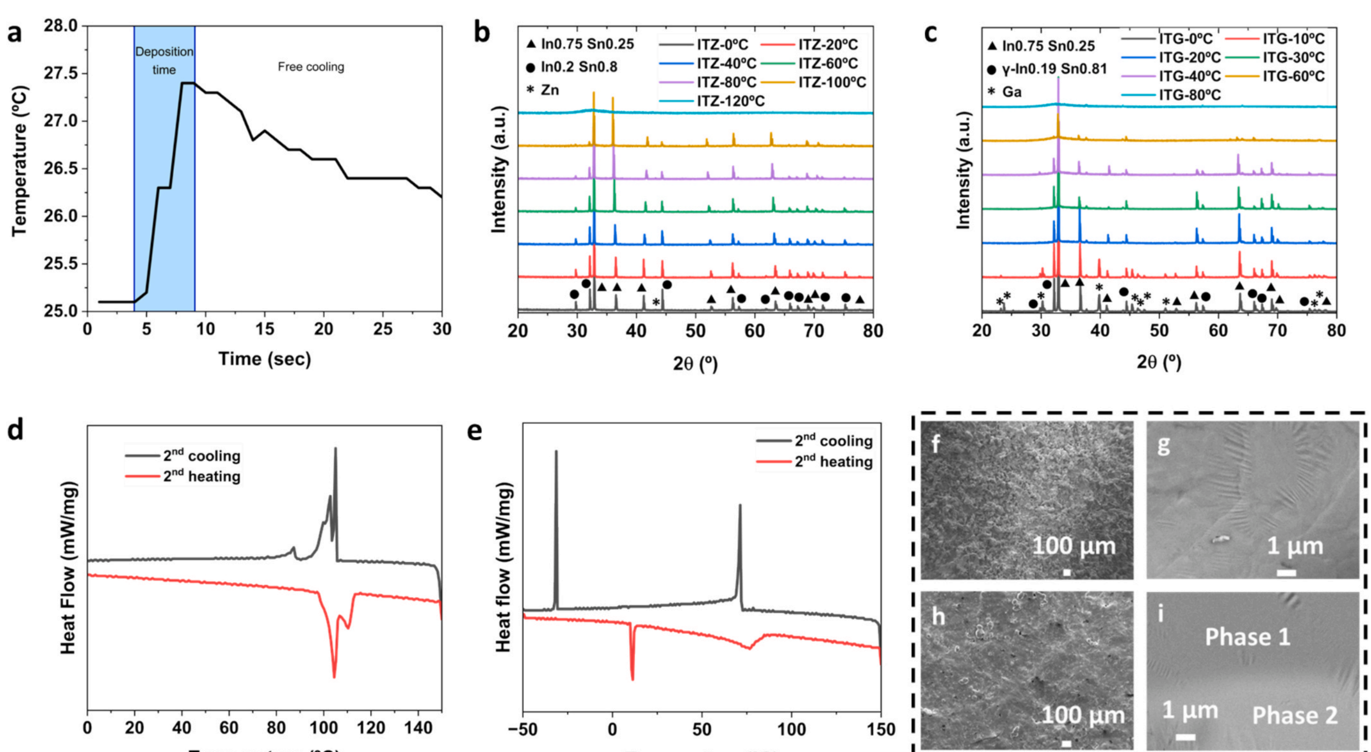

Fig. 2. (a) Surface temperature monitoring of the sample during the deposition of the metallic layer. (b) Sum diffractogram of sample ITZ at different temperatures between 0 and 120 °C. (c) XRD results for the ITG alloy performed between 0 and 80 °C. (d) DSC curves of ITZ alloy between 0 °C and 150 °C and (e) ITG alloy between −50 °C and 150 °C. (f, g) Surface micrographs of ITZ and ITG alloys, showing the roughness of the layers. (h, i) Backscattered electron micrographs for ITZ and ITG, respectively.

Cmca phase (PDF#01-089-2735), a (γ) (tin rich) (In,Sn), hexagonal *P6/mmm* (04-007-5069) and a (β)(indium rich) (In,Sn) tetragonal *I4/mmm* (PDF#04-004-7736). Fourth minor crystalline phase was identified (**Fig. S2**), very probably corresponding to the silver Ag on the bottom of the sample, observed since very probably when entering, fast, the sample at 0 °C if was not axially correctly placed and the X-ray beam impinges a bit in the bottom upper silver sheet. At higher temperatures to 10 °C two crystalline structural types (phases) have been identified: (γ) (tin rich) (In,Sn), hexagonal *P6/mmm* and (β)(indium rich) (In,Sn) tetragonal *I4/mmm*. Moreover, there is clearly an amorphous phase (very probably the Ga liquid phase) noticed by a very wide peak (halo) cantered around 34° (See **Fig. S2** for a clearest observation). Finally, at 80 °C, the alloy melted only being observable an amorphous phase.

The thermal behavior of the metal alloys was investigated using differential scanning calorimetry (DSC), with the results shown in Fig. 2d and e. The thermogram of the ITZ alloy (Fig. 2d), recorded between 0 and 150 °C, reveals a single endothermic transition near 109 °C, attributed to the melting and solidification of its main crystalline phases. In contrast, the ITG alloy (Fig. 2e) exhibits two distinct thermal events: the first at approximately 11 °C, corresponding to the melting of the orthorhombic Ga-rich phase (Cmca), and a second, broader transition at 75 °C, associated with the tin-rich (γ, hexagonal P6/mmm) and indium-rich (β, tetragonal I4/mmm) phases. A pronounced supercooling effect is observed in the gallium-based phase, with recrystallization occurring only below −31 °C, consistent with the behavior of Ga-based systems reported in the literature [29].

3.3. Morphological characterization

In Fig. 2f and h, the morphology of the ITZ alloy are observed. In the backscattered electron micrograph (Fig. 2h), the compositional homogeneity of the layer is observed. Additional geometrical characterization of the sprayed electrodes, cross-sectional SEM, and optical profilometry measurements, is provided in Supporting Information (**Section S3**). A high surface roughness is noted, partly due to a higher melting point, which probably causes the droplets to solidify as they approach the substrate obtaining an average rugosity (Ra) of 43.864 μm. Fig. 2g shows a homogeneous layer of the ITG alloy deposited on an FTO glass with Ra 11.186 μm. The backscattered electron micrograph of the ITG (Fig. 2i) shows two different phases, the darkest richest in gallium probably being the Gallium phase and the brighter area richest in tin and indium. Energy-dispersive X-ray spectroscopy (EDX) (**Supporting information S4**) was used to determine the atomic percentage of each phase, thereby confirming the nominal compositions used during alloy synthesis.

Beyond compositional verification, the EDX analysis also provides insight into the surface chemistry of the deposited films. During droplet transport from the airbrush to the substrate, the molten alloy is exposed to ambient atmosphere, and partial surface oxidation is therefore expected. In particular, for the ITG alloy, gallium is well known to rapidly form a thin native Ga_2O_3 layer upon contact with oxygen [30]. This oxidation process is typically self-limiting and confined to a nanometric surface film that acts as a diffusion barrier, preventing further oxidation of the metallic core. Upon impact, the droplets undergo rapid solidification (fully in the case of ITZ and partially in ITG), which further restricts oxygen diffusion slowing down the development of oxide regions. The EDX spectra shown in **Fig. S4** reveal weak or non-quantifiable oxygen signals for both the ITZ and ITG alloy, surface oxidation is also expected, however, any nanometric oxide layers formed appear to remain below the effective detection sensitivity of SEM-EDX and do not produce intense or quantifiable oxygen signals for the samples deposited less than 24 h before the analysis. In contrast, EDX measurements performed on samples stored under ambient conditions for six months (Supporting Information, **Fig. S4g–h**) show a noticeable increase in oxygen signal. This indicates progressive surface oxidation that may influence surface contact quality, particularly in regions directly exposed to air.

3.4. Application to perovskite solar cells

To assess electrical performance, specific contact resistivity between the metallic films and FTO substrates were measured using the transmission line method (TLM). For each alloy, three samples were prepared by depositing the metal through precision-cut masks that created a seven-fingered pattern with spacing from 0.1 to 0.35 mm. The design is schematically shown in Fig. 3a. The masks were fabricated using a 355 nm UV laser, and the actual gap dimensions were verified by SEM, revealing a consistent 35 μm reduction relative to the design due to the laser spot diameter (**Fig. S5**, Supporting Information). This correction was included in the subsequent calculations.

From the measured resistance values as a function of finger spacing, the sheet resistance and specific contact resistivity were extracted. Representative resistance versus distance plots are presented in **Fig. S6** (Supporting Information). The calculated values are summarized in Table 2, which includes reference data for 100 nm thermally evaporated silver and commercial micrometric–milimetric printed silver ink layers. Among the materials tested, the ITG alloy demonstrated the lowest specific contact resistivity (0.43 ± 0.11 mΩ·cm^2), approaching the performance of evaporated silver (0.37 ± 0.11 mΩ·cm^2) and significantly outperforming both silver ink and the ITZ alloy. These superior results can be attributed to the formation of a more continuous film compared to silver ink, as the process does not rely on solvents or particle sintering. Additionally, the smoother surfaces generated during deposition, as observed in the SEM micrographs, enhance the contact area between the metal and the FTO layer.

Fig. 3b–e summarizes the photovoltaic performance of bromine-based perovskite solar cells fabricated using identical device architectures and completed with different back electrodes: thermally evaporated silver, MMS-deposited ITG, and MMS-deposited ITZ. The corresponding J–V curves for representative devices are shown in Fig. 3b–d, while the extracted photovoltaic parameters are listed in Table 3. To assess the impact of the metallization strategy under controlled conditions, multiple devices were fabricated on the same substrates and processed in parallel, differing only in the contact material. Fig. 3e shows the statistical distribution of power conversion efficiencies obtained for each electrode type. Devices incorporating ITZ contacts exhibit a broader performance dispersion, mainly associated with one lower-performing cell, which is consistent with the higher variability inferred from the specific contact resistivity values obtained by TLM analysis.

As expected, devices completed with thermally evaporated silver exhibit slightly higher average performance, reflecting the well-established quality of vacuum-deposited contacts. However, the differences in photovoltaic parameters between Ag and MMS-based contacts remain limited within the same device architecture, with average power conversion efficiencies differing by only a few tenths of a percent. These results indicate that MMS-deposited ITG and ITZ contacts provide electrically functional back electrodes for perovskite solar cells, while remaining in the solid state under typical device operating temperatures. Although long-term operation could potentially lead to more pronounced degradation effects related to metal migration or interfacial interactions inherent to the alloy composition, the present results demonstrate the practical viability of the MMS approach for the rapid and straightforward fabrication and testing of photovoltaic devices at the laboratory scale.

3.5. Conductive circuits

The applicability of the MMS method was further validated by fabricating conductive patterns to assess its feasibility across different device configurations. These experiments aim to demonstrate the robustness and versatility of the deposition approach under representative electrical and mechanical constraints. The resulting electrical and mechanical response is primarily governed by the alloy composition,

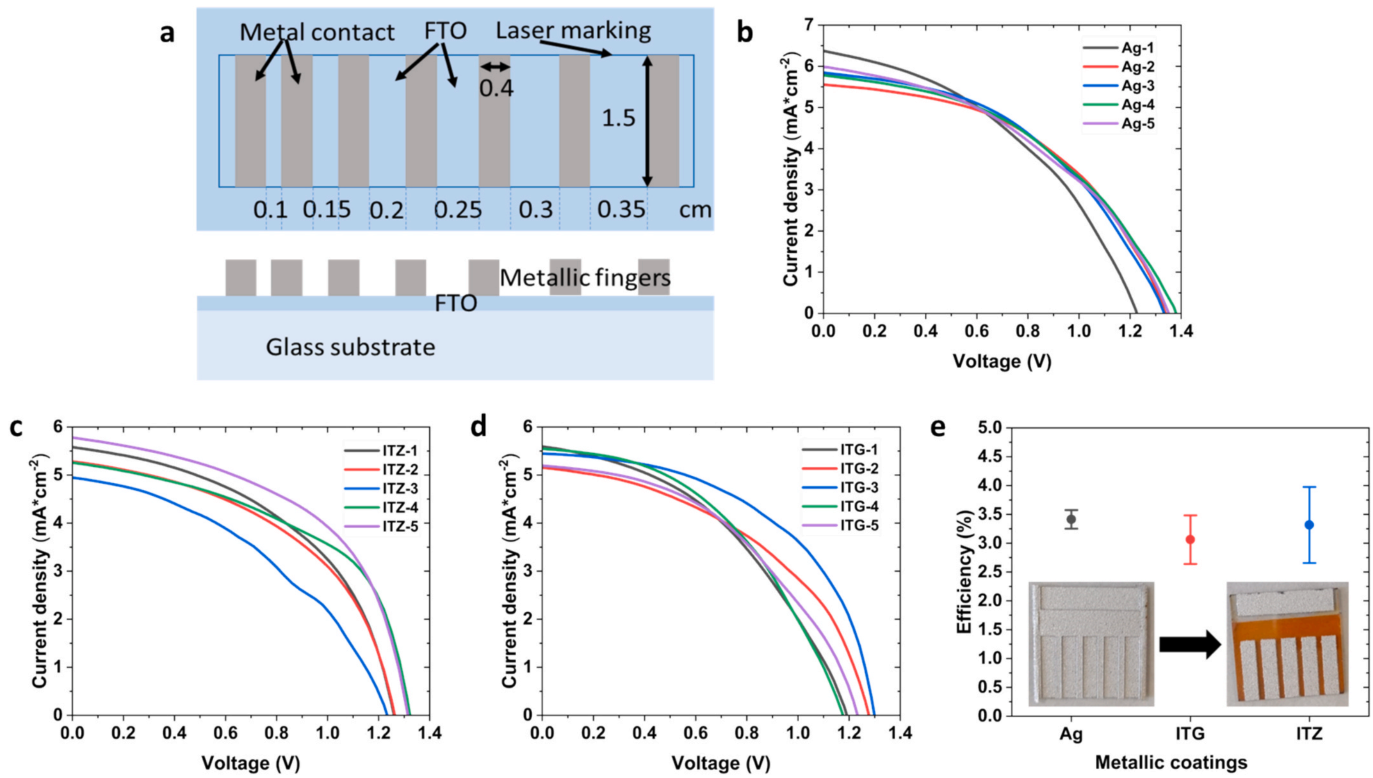

Fig. 3. (a) Scheme of the pattern used for the TLM measurements with a representation of the top view and cross section. J-V curves of the 5 different $FAPbBr_3$ devices curves metallized with the (b) evaporated Ag, (c) ITG and (d) ITZ alloys. (f) Dispersion of the obtained efficiencies for each device with an inset of the device with and without the mast just after the deposition of the ITZ metallic film.

Table 2
Specific contact resistivity values for evaporated silver, silver ink, ITZ and ITG alloys.

Sample	Rs/W (Ω cm^{-1})	Lt (cm)	Rc (Ω)	Rs (FTO) (Ω/sq)	Specific contact resistivity (mΩ cm^2)
Ag (evaporated)	4.74 ± 0.03	0.01 ± 0.01	0.034 ± 0.005	7.1 ± 0.1	0.37 ± 0.11
Ag ink	4.66 ± 0.10	0.014 ± 0.002	0.065 ± 0.010	7.0 ± 0.2	1.4 ± 0.5
ITZ	4.6 ± 0.2	0.015 ± 0.003	0.069 ± 0.013	7.0 ± 0.2	1.6 ± 0.7
ITG	4.80 ± 0.08	0.010 ± 0.001	0.037 ± 0.005	7.2 ± 0.1	0.43 ± 0.11

Table 3
Solar cells I-V parameters for each of the devices of Fig. 3b,3c and 3d.

Sample	Jsc (mA cm^{-2})	Voc (V)	FF (%)	Eff (%)
$FAPbBr_3$–Ag	5.9 ± 0.3	1.32 ± 0.06	43.8 ± 2.5	3.4 ± 0.1
$FAPbBr_3$–ITG	5.4 ± 0.2	1.23 ± 0.05	46.0 ± 3.4	3.1 ± 0.3
$FAPbBr_3$–ITZ	5.4 ± 0.3	1.28 ± 0.04	48.0 ± 4.3	3.3 ± 0.5

while MMS functions as a general metallization platform compatible with a broad range of low-melting-point materials.

Fig. 4 summarizes the electrical performance under the various tests conducted. In Fig. 4a, the resistance of MMS-printed circuits with a length of 10 cm and different line widths is shown, enabling determination of the minimum printable resolution. The minimum continuous conductive line was achieved at 150 μm, exhibiting a resistance of 0.784 Ω. Below this threshold, at 100 μm, the printed features displayed either insulating behavior or resistances in the MΩ range, indicating loss of electrical continuity. This loss of continuity is primarily attributed to the current atomization and stencil-lithography limits. Using a 0.5 mm nozzle at a 10 cm stand-off distance produces droplets and overspray scales that become comparable to ~150 μm features; as a result, the deposit transitions from a continuous wetting/coalescence film to a segmented droplet chain with oxide/void gaps, leading to insulating segments or MΩ-level resistances. From these measurements also an apparent electrical resistivity of near 30 μΩ·cm was estimated for the electrodes.

Mechanical durability was evaluated through bending and stretching tests (Fig. 4b). For bending reliability, both alloys were deposited on a paper foil. S-bend cyclic tests revealed a sharp degradation in conductivity for the ITZ alloy, which lost nearly all electrical performance after ~100 cycles. In contrast, the ITG alloy demonstrated remarkable stability, after a slight decrease in resistance during the first cycles, the values stabilized after approximately 300 cycles. This enhanced bending endurance is attributed to the coexistence of a solid and a liquid phase within ITG, which accommodates mechanical deformation.

Stretching durability was also investigated for the ITG alloy as can be seen in Fig. 4c and d. Two distinct protocols were performed. First, cyclic stretching to 20% strain for 1000 cycles revealed a progressive resistance increase from 0.3295 Ω to 2.1264 Ω, with the most rapid degradation occurring in the initial cycles. SEM micrograph confirms a clear crack formation in the circuit after 1000 cycles (**Fig. S7**). Second, monotonic stretching tests at fixed strain values between 5% and 20% confirmed the ability of ITG-based circuits to maintain conductivity under significant elongation, demonstrating their potential for application in stretchable and wearable electronics.

To further illustrate the versatility of the MMS process, proof-of-concept devices were fabricated on unconventional substrates. Fig. 5a shows a simple circuit printed on paper, powered by a 3 V battery and

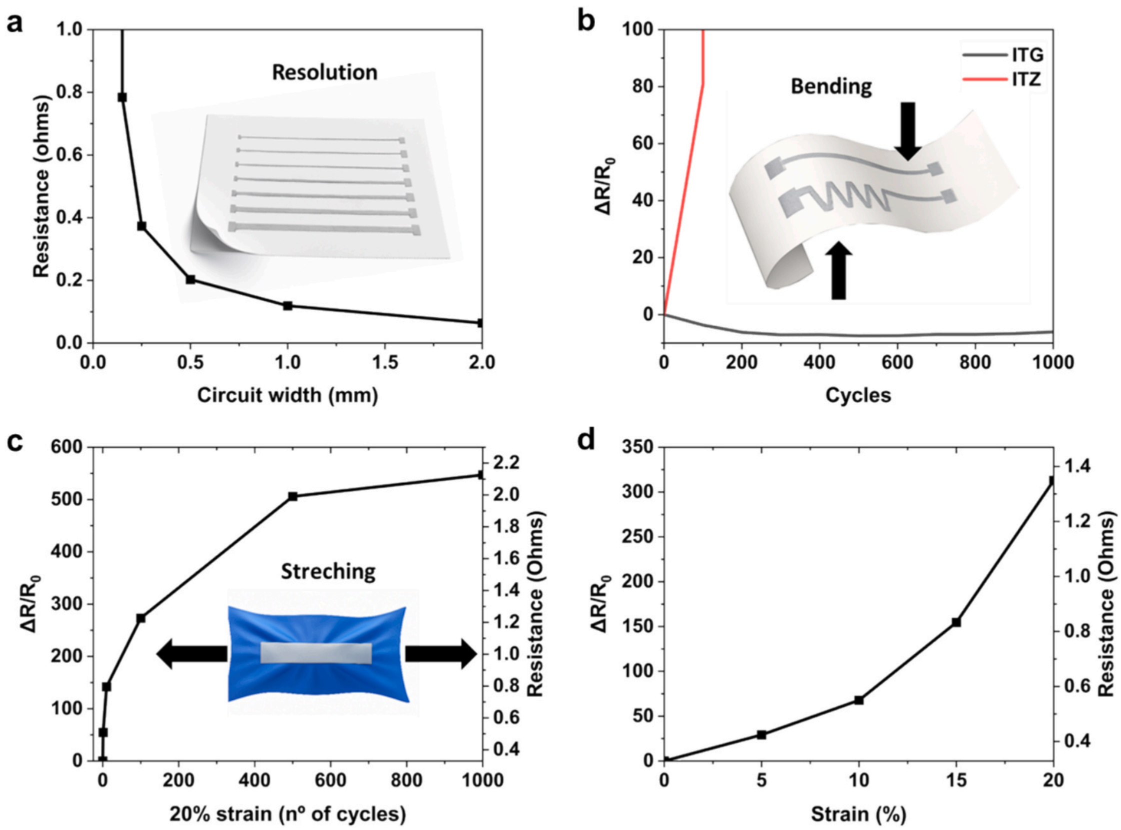

Fig. 4. Electrical and mechanical reliability of MMS-printed circuits. (a) Resistance of 10 cm long printed lines with different widths, showing the minimum resolution achievable by the method. (b) Evolution of resistance during S-bend cyclic tests, comparing ITZ and ITG alloys. (c) Resistance variation of ITG circuits under 1000 stretching cycles at 20% strain. (d) Resistance response of ITG circuits under monotonic stretching at strain levels between 5% and 20%.

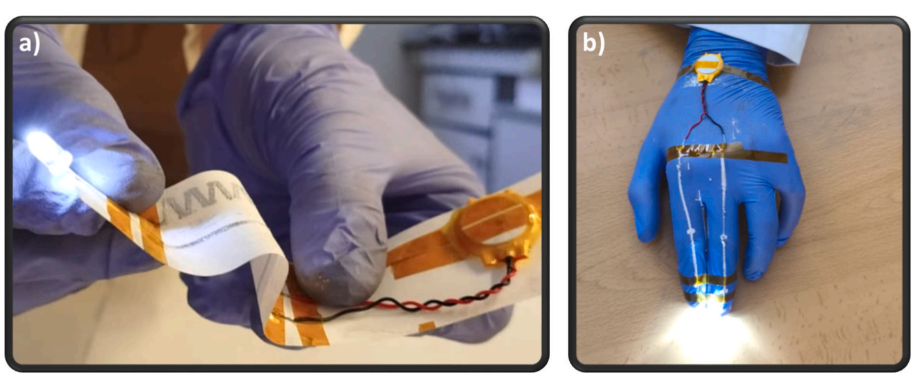

Fig. 5. Proof-of-concept MMS-based devices fabricated on unconventional substrates. (a) Circuit printed on paper powered by a 3 V battery and connected to a white LED. (b) Conductive pattern deposited on a nitrile glove driving a white LED at the fingertip.

driving a white LED, while Fig. 5b demonstrates the direct integration of a conductive pathway onto a nitrile glove to operate an LED at the fingertip. These examples highlight the method's ability to produce functional electronic circuits on both rigid and highly deformable substrates, expanding its applicability toward low-cost, flexible, and wearable electronics. **Supplementary Videos 2 and 3** provide dynamic demonstrations of these devices in operation under bending and stretching, confirming their mechanical robustness and functionality under real use conditions.

3.6. Environmental assessment

The environmental analysis of the MMS method was applied to compare the environmental impacts of silver electrodes for bromide perovskites, fabricated via vacuum evaporation [31], against ITG electrodes, fabricated via the MMS method. Since the energy efficiencies obtained in this application are similar (Table 2), a functional unit of 1 cm^2 of electrode was established. The environmental impacts associated with the synthesis and deposition processes were evaluated using Life Cycle Assessment (LCA) methodology, conducted in accordance with EN-ISO standards (14040/14044).

Only the back contact layer of the solar cell was considered in this analysis. The remaining layers are identical for both methods and were therefore excluded from the comparative assessment. Life cycle inventories and impact evaluations, obtained using the Environmental Footprint (EF) 3.1 v 1.03 method and SimaPro Craft v 10.2.0.3 software, are presented in the **Supplementary Information 8**.

The MMS method for ITG deposition reduces energy consumption by a factor of nearly 40, see Fig. 6a. This calculation encompasses the deposition process itself, the heating required to melt the metal, and the recycling of recovered ITG. This significant reduction in energy consumption leads to substantial decreases in environmental impacts, as illustrated in Fig. 6b, c.

The climate change impact of the ITG electrode is 63% of that observed for the silver electrode, Fig. 6b. This is primarily due to energy savings compensating for the higher impact of the materials used. Conversely, the recycling of recovered material and waste treatment has a negligible influence on this impact category. The quantity of ITG deposited and lost is 15 times greater than the quantity of silver deposited and lost. In this initial investigation of the ITG electrode in perovskites, an airbrush nozzle with a 0.5 mm diameter was utilized. Future experimentation with smaller diameter nozzles could lead to reduced material consumption and losses. Furthermore, using a smaller initial quantity would decrease the energy required for heating and recycling, although electricity consumption might increase slightly due to the need for higher pressure. Notably, both methods exhibit high loss percentages: 96% for the vacuum evaporation of silver and 49% for the MMS deposition of ITG.

Fig. 6c shows the prioritized impact categories for the silver electrode derived from the EF3.1 normalization and weighting set. The most significant categories include resource use (minerals and metals), climate change, freshwater eutrophication, resource use (fossils) and acidification. Collectively, these indicators represent 95% of the total weighted impact. Detailed weighted impact values are provided in **Table S4**. In all these categories, the ITG electrode exhibits impacts that are less than 65% of those associated with the silver electrode. From a broader economic and environmental perspective, silver represents a particularly stringent reference material, as alternative metals widely employed in industrial metallization, such as aluminum or copper, generally exhibit lower material costs and reduced environmental burdens. Although this alternative metallization strategies generally involves additional technical constraints (e.g., oxide formation and interfacial resistance in aluminum, or the need for buffer layers and encapsulation in copper) [32]. Accordingly, the relative advantages observed for the MMS approach when benchmarked against silver may be less pronounced when such alternative contact metals are considered.

However, the higher material consumption of the ITG electrode results in greater impacts in the ecotoxicity and human toxicity categories (both carcinogenic and non-carcinogenic) see **Table S3** and **Fig. S8**. A further limitation in these categories is the absence of characterization factors for indium and gallium, and the partial lack thereof for tin. Consequently, the impacts resulting from the emission of these materials during extraction, processing, and end-of-life are not fully accounted for.

Finally, gallium, a component of ITG, is included in the European Union's list of Critical Raw Materials [33], given that 94% of its supply originates from China. While the use of alternative alloy compositions such as ITZ can partially mitigate supply-chain risks by eliminating gallium, indium availability and long-term sustainability remain a concern. From a metallurgical perspective, achieving melting temperatures below 100 °C without relying on indium, gallium, or toxic elements such as cadmium or mercury is highly restrictive. To the best of our knowledge, indium-free low-melting alternatives are essentially limited to Bi–Pb–Sn systems, which avoid critical elements but introduce lead-related environmental and regulatory trade-offs, or to higher-melting Bi–Sn-based alloys that are less suitable for low-temperature electronic contacts [34].

3.7. Techno-economic comparison with conventional metallization methods

To contextualize the performance and practicality of the Melted Metal Spray (MMS) technique, a comparative analysis with other common metallization methods was conducted. Table 4 summarizes key parameters such as equipment cost, deposition time, and maximum substrate temperature for a range of conventional and alternative techniques, including thermal evaporation, sputtering, inkjet printing, and chemical plating between others. As seen in the table, most high-quality methods operate under vacuum conditions and require significant investment in equipment, along with extended processing times. In contrast, MMS achieves similar or lower deposition times (<1 min) using significantly simpler and more affordable equipment (100–1000 €) and operating under ambient conditions at a substrate temperature of near 30 °C. Unlike other low-cost approaches such as spray coating or ink-based methods, which risk degrading sensitive materials like perovskites, because their high-temperature under air, MMS offers a thermally gentle alternative while preserving electrical contact quality. This positions MMS as a viable solution for laboratories aiming to fabricate functional photovoltaic devices or for rapid prototyping

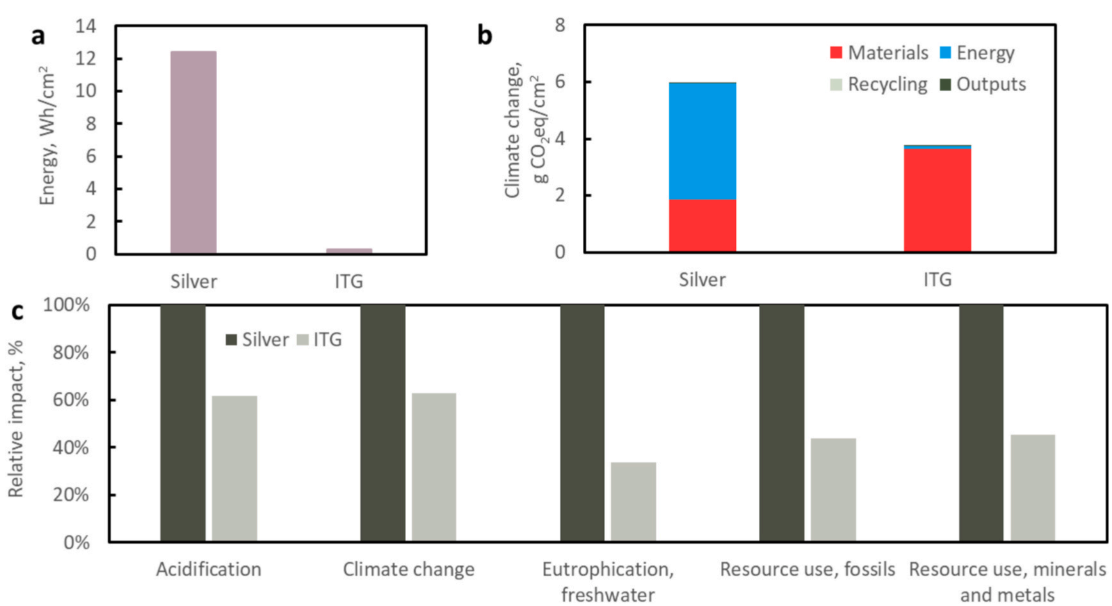

Fig. 6. Environmental comparison between the silver electrode and ITG. a) Comparison of energy consumption during deposition, accounting for heating and ITG electrode recycling; b) Climate change impact categorized by materials, energy, recycling, and outputs; c) Relative comparison of the most significant categories according to the EF 3.1 method.

Table 4
Comparative table of the cost, temperature and time required for different deposition methods of metallic layers.

Deposition technique	Required equipment	Equipment Price*	Deposition time* (min)	Sample max. Temperature* (°C)
Thermal evaporation [35]	Vacuum thermal evaporator + vacuum pump	10,000–50,000€	40	35
Sputtering [36]	Magnetron Sputtering + Vacuum pump	50,000–100,000€	80	150
Laser ablation [37,38]	Laser + Vacuum chamber + vacuum pump	100,000–250,000€	75	RT
Atomic layer deposition [39]	Atomic layer deposition + vacuum pump	100,000–200,000€	270	100
Inkjet printing [20,21]	Inkjet	50,000–100,000€	22	150
Ink [19]	Brush	0-100€	22	150
Spray coating [40,41]	Spray gun or coater	100–50,000€	1030	100
Thermal spray coating [42,43]	Thermal spray gun	50,000–150,000€	1	100
Electrodeposition [23]	Potenciostat galvanostat	1000–20,000€	5	RT
Chemical plating [24]	Plating	0–100€	20	RT
This work	**Spray gun or coater + hot plate**	**100–1000€**	**1**	**28**

* The price, time, and temperature were obtained from various bibliographic sources and companies, aiming to present the methods in a favourable context. The data serve simply as a guideline for classification purposes, and exceptions may exist.

circuits without the infrastructure typically associated with metallic film deposition systems.

It is also worth noting that, while the simplicity of the MMS setup and its low capital cost make it particularly attractive for rapid prototyping and laboratory-scale fabrication, the relatively larger amount of metal deposited per sample and in this case the use of critical materials like Gallium may limit its economic competitiveness under large-scale production scenarios. In contrast other mature vacuum-based metallization technologies, such as roll-to-roll vacuum deposition on polymer substrates, are highly optimized for material efficiency and throughput, and can therefore be cost-effective at industrial scale despite their higher initial infrastructure requirements.

4. Conclusions

This work presents and validates a novel, rapid, and low-temperature metallization technique, Melted Metal Spray (MMS), for forming electrical contacts in electronic devices. By employing low-melting-point alloys, the process enables metal deposition in less than 10 s while increasing substrate temperatures below 3 °C, a key advantage for thermally sensitive materials such as lead-halide perovskites or polymeric substrates. Unlike conventional metallization approaches that require vacuum systems, long processing times, or aggressive chemical environments, MMS operates under ambient conditions using simple and low-cost equipment.

Electrical characterization confirmed that the specific contact resistivity of the MMS-deposited ITG/FTO interface (0.43 ± 0.11 mΩ·cm^2) is comparable to thermally evaporated silver, while offering greater process simplicity and material recyclability. Successful integration of the technique in perovskite solar cells demonstrated power conversion efficiencies on par with conventional contacts, confirming its functional viability. However, morphological analysis revealed that alloys with melting points above ~110 °C may yield lower-quality films due to premature solidification of droplets upon impact.

Life Cycle Assessment confirms that the MMS method for ITG deposition significantly outperforms vacuum-evaporated silver, driven by a nearly 40-fold reduction in energy consumption and a decrease in climate change impact to 63% of the standard method. Consequently, MMS presents a sustainable alternative.

Beyond the quantitative metrics, MMS has implications for device design. The ability to form metallic back contacts rapidly, at ambient atmosphere, and with minimal thermal impact enables late-stage integration without imposing additional thermal constraints on multilayer stacks. This is particularly relevant for perovskite and flexible electronic architectures, where metallization often represents the most infrastructure-intensive and thermally critical step. By removing the need for vacuum systems and high-temperature post-treatments, MMS expands the processing flexibility available during device fabrication.

At the same time, certain limitations must be acknowledged. The technique is currently better suited for rapid prototyping and small-scale fabrication than for optimized large-scale industrial production. Moreover, MMS is restricted to low-melting-point alloys, which limits the available material palette and constrains photovoltaic applications mainly to p–n–metal configurations compatible with relatively low work-function contacts.

Overall, MMS represents a simple, versatile, and low-cost metallization strategy that bridges the gap between high-performance device fabrication and accessible laboratory processes. While not intended to replace established industrial vacuum lines, it provides a practical alternative for decentralized development, flexible electronics, and rapid iteration of electronic and photovoltaic devices.

CRediT authorship contribution statement

Samuel Porcar-Garcia: Writing – original draft, Methodology, Investigation, Formal analysis, Conceptualization. **Olfa Selmi:** Investigation, Formal analysis. **Abderrahim Lahlahi:** Investigation, Data curation. **Santiago Toca:** Investigation, Data curation. **Antoni Merin:** Writing – original draft, Formal analysis. **Xavier Alcobe:** Writing – review & editing, Supervision. **Sofia Masi:** Writing – review & editing, Supervision. **Rosario Vidal:** Writing – original draft, Formal analysis, Data curation. **Iván Mora-Seró:** Supervision. **Jaime González-Cuadra:** Writing – review & editing, Supervision. **Juan Bautista Carda:** Validation, Supervision, Funding acquisition.

Declaration of competing interest

The authors declare that they have no known competing financial interests or personal relationships that could have appeared to influence the work reported in this paper.

Acknowledgments

The authors gratefully acknowledge the financial and institutional support that made this work possible. Jaime González Cuadra acknowledges the postdoctoral contract (reference CIAPOS/2023/425) and the predoctoral contract (reference CIACIF/2022/277), both co-funded by the Generalitat Valenciana (Valencian Community Government) and the European Social Fund (FSE+). Authors acknowledges financial support for project PRINT-P (MFA/2022/020) that forms part of the Advanced Materials programme and was supported by MCIN (Spain) with funding from European Union NextGenerationEU (PRTR-C17.I1) and by Generalitat Valenciana and also to the Project CLUSKER: INNEST/2024/420 financed by the "Instituto Valenciano de Competitividad Empresarial" (IVACE). This work was also supported by the Ministry of Science and Innovation of Spain MCIN/AEI/https://doi.org/10.13039/501100011033/ and by FEDER "Una manera de hacer Europa" under Project ConFlex (PID2023-151880OB-C33). O. S. acknowledges financial support from Comunidad Valenciana through the program GRISOLIA (CIGRIS/2022/122). The authors also thank the

Scientific Instrumentation Services (SCIC) at the Universitat Jaume I (Spain) for providing access to facilities and equipment essential for sample characterization, and the Càtedra d'Innovació Ceràmica "Ciutat de Vila-real" de la Universitat Jaume I for their support.

Appendix A. Supplementary data

Supplementary data to this article can be found online at https://doi.org/10.1016/j.matdes.2026.115812.

Data availability

Data will be made available on request.

References

[1] N.A. Utama, A.M. Fathoni, M.A. Kristianto, B.C. McLellan, The end of fossil fuel era: supply-demand measures through energy efficiency, Procedia Environ. Sci. 20 (2014) 40–45, https://doi.org/10.1016/j.proenv.2014.03.007.
[2] P.J. Megía, A.J. Vizcaíno, J.A. Calles, A. Carrero, Hydrogen production technologies: from fossil fuels toward renewable sources. A mini review, Energy Fuels 35 (2021) 16403–16415, https://doi.org/10.1021/acs.energyfuels.1c02501.
[3] A. Bouich, I.G. Pradas, M.A. Khan, Y.H. Khattak, Opportunities, challenges, and future prospects of the solar cell market, Sustainability 15 (2023) 15445, https://doi.org/10.3390/su152115445.
[4] C.R. Kumar J, M.A. Majid, Renewable energy for sustainable development in India: current status, future prospects, challenges, employment, and investment opportunities, Energy Sustain. Soc. 10 (2020) 2, https://doi.org/10.1186/s13705-019-0232-1.
[5] A. Urbina, The balance between efficiency, stability and environmental impacts in perovskite solar cells: a review, J. Phys. Energy 2 (2020) 022001, https://doi.org/10.1088/2515-7655/ab5eee.
[6] A. Uddin, M.B. Upama, H. Yi, L. Duan, Encapsulation of organic and perovskite solar cells: a review, Coatings 9 (2019) 65, https://doi.org/10.3390/coatings9020065.
[7] S.Y. Kim, C.C.F. Kumachang, N.Y. Doumon, Characterization tools to probe degradation mechanisms in organic and perovskite solar cells, Sol. RRL 7 (2023) 2300155, https://doi.org/10.1002/solr.202300155.
[8] J. Werner, B. Niesen, C. Ballif, Perovskite/silicon tandem solar cells: marriage of convenience or true love story? – an overview, Adv. Mater. Interfaces 5 (2018) 1700731, https://doi.org/10.1002/admi.201700731.
[9] M.G. Buonomenna, Inorganic thin-film solar cells: challenges at the terawatt-scale, Symmetry 15 (2023) 1718, https://doi.org/10.3390/sym15091718.
[10] M.N. Chaudhari, Thin film deposition methods: a critical review, Int. J. Res. Appl. Sci. Eng. Technol. 9 (2021) 5215–5232, https://doi.org/10.22214/ijraset.2021.36154.
[11] Y. Wang, L. Duan, M. Zhang, Z. Hameiri, X. Liu, Y. Bai, X. Hao, PTAA as efficient hole transport materials in perovskite solar cells: a review, Sol. RRL 6 (2022) 2200234, https://doi.org/10.1002/solr.202200234.
[12] Y. Yao, W.-L. Hsu, M. Dagenais, High-efficiency perovskite solar cell based on sequential doping of PTAA, IEEE J. Photovolt. 9 (2019) 1025–1030, https://doi.org/10.1109/JPHOTOV.2019.2910236.
[13] Y. Zeng, C.-W. Peng, W. Hong, S. Wang, C. Yu, S. Zou, X. Su, Review on metallization approaches for high-efficiency silicon heterojunction solar cells, Trans. Tianjin Univ. 28 (2022) 358–373, https://doi.org/10.1007/s12209-022-00336-9.
[14] S. Tepner, A. Lorenz, Printing technologies for silicon solar cell metallization: a comprehensive review, Prog. Photovolt. Res. Appl. 31 (2023) 557–590, https://doi.org/10.1002/pip.3674.
[15] A. Ebong, N. Chen, Metallization of crystalline silicon solar cells: a review, in: High Capacity Opt. Netw. Emerging Enabling Technol., IEEE, Istanbul, Turkey, 2012, pp. 102–109, https://doi.org/10.1109/HONET.2012.6421444.
[16] Z. Wang, M. Lyu, B.W. Zhang, M. Xiao, C. Zhang, E. Han, L. Wang, Thermally evaporated metal halide perovskites and their analogues: film fabrication, applications and beyond, Small Methods 9 (2025) 2301633, https://doi.org/10.1002/smtd.202301633.
[17] Z. Fekkai, Optical, morphological and electrical properties of silver and aluminium metallization contacts for solar cells, Am. J. Mod. Phys. 3 (2014) 45, https://doi.org/10.11648/j.ajmp.20140302.13.
[18] R. Wu, S. Sun, D. Liu, J. Lai, Y. Yu, S. Hu, J. Liu, S. Li, Y. Li, L. Li, M. Jiang, C. Liu, J. Deng, C. Wang, Rapid evaporation of a metal electrode for a high-efficiency perovskite solar cell, Polymers 16 (2023) 94, https://doi.org/10.3390/polym16010094.
[19] R. Yang, E. Mazalan, K.T. Chaudhary, Z. Haider, J. Ali, Non-vacuum deposition methods for thin film solar cell, AIP Conf. Proc. 1824 (2017) 030018, https://doi.org/10.1063/1.4978836.
[20] Y. Sui, C.A. Zorman, Review—Inkjet printing of metal structures for electrochemical sensor applications, J. Electrochem. Soc. 167 (2020) 037571, https://doi.org/10.1149/1945-7111/ab721f.
[21] S. Kholghi Eshkalak, A. Chinnappan, W.A.D.M. Jayathilaka, M. Khatibzadeh, E. Kowsari, S. Ramakrishna, A review on inkjet printing of CNT composites for smart applications, Appl. Mater. Today 9 (2017) 372–386, https://doi.org/10.1016/j.apmt.2017.09.003.
[22] K.A. Kravanja, M. Finšgar, A review of techniques for the application of bioactive coatings on metal-based implants to achieve controlled release of active ingredients, Mater. Des. 217 (2022) 110653, https://doi.org/10.1016/j.matdes.2022.110653.
[23] E.C. Gugua, C.O. Ujah, C.O. Asadu, D.V. Von Kallon, B.N. Ekwueme, Electroplating in the modern era, improvements and challenges: a review, Hybrid Adv. 7 (2024) 100286, https://doi.org/10.1016/j.hybadv.2024.100286.
[24] F. Muench, Electroless plating of metal nanomaterials, ChemElectroChem 8 (2021) 2993–3012, https://doi.org/10.1002/celc.202100285.
[25] H. Assadi, F. Gärtner, T. Stoltenhoff, H. Kreye, Bonding mechanism in cold gas spraying, Acta Mater. 51 (2003) 4379–4394, https://doi.org/10.1016/S1359-6454(03)00274-X.
[26] E.B. Secor, Principles of aerosol jet printing, Flex. Print. Electron. 3 (2018) 035002, https://doi.org/10.1088/2058-8585/aace28.
[27] Q. Zhang, Y. Gao, J. Liu, Atomized spraying of liquid metal droplets on desired substrate surfaces as a generalized way for ubiquitous printed electronics, Appl. Phys. A 116 (2014) 1091–1097, https://doi.org/10.1007/s00339-013-8191-4.
[28] T. Neumann, B. Kara, Y. Sargolzaeiaval, S. Im, J. Ma, J. Yang, M. Ozturk, M. Dickey, Aerosol spray deposition of liquid metal and elastomer coatings for rapid processing of stretchable electronics, Micromachines 12 (2021) 146, https://doi.org/10.3390/mi12020146.
[29] S. Handschuh-Wang, T. Gan, M. Rauf, W. Yang, F.J. Stadler, X. Zhou, The subtle difference between Galinstan (R) and eutectic GaInSn, Materialia 26 (2022) 101642, https://doi.org/10.1016/j.mtla.2022.101642.
[30] M.D. Dickey, R.C. Chiechi, R.J. Larsen, E.A. Weiss, D.A. Weitz, G.M. Whitesides, Eutectic Gallium-Indium (EGaIn): a liquid metal alloy for the formation of stable structures in microchannels at room temperature, Adv. Funct. Mater. 18 (2008) 1097–1104, https://doi.org/10.1002/adfm.200701216.
[31] O. Selmi, A. Lorusso, M. Mazzeo, J.-A. Alberola-Borràs, R. Vidal, E.M. Barea, R. S. Sánchez, I. Mora-Seró, S. Masi, Spectroscopic matching in semitransparent solar cells with I–Br mixed halide perovskite and DMD electrode, Mater. Adv. 6 (2025) 7231–7242, https://doi.org/10.1039/D5MA00972C.
[32] S. Cao, J. Han, X. Zhao, Y. Yu, P. Gao, Copper contact for perovskite solar cells: properties, interfaces, and scalable integration, Adv. Energy Sustain. Res. (2025) e202500380, https://doi.org/10.1002/aesr.202500380.
[33] Study on the Critical Raw Materials for the EU 2023 – Final Report, Publications Office of the European Union, Luxembourg, 2023. https://doi.org/10.2873/725585.
[34] I. Manasijevic, L.J. Balanovic, D. Minic, M. Gorgievski, U. Stamenkovic, Investigation of latent heat of melting and thermal conductivity of the low-melting Bi-Sn-Zn eutectic alloy, Met. Mater. 57 (2020) 267–273, https://doi.org/10.4149/km_2019_4_267.
[35] R. Abermann, H.P. Martinz, R. Kramer, Thermal effects during the deposition of thin silver, gold and copper films and their influence on internal stress measurements, Thin Solid Films 70 (1980) 127–137, https://doi.org/10.1016/0040-6090(80)90420-4.
[36] M.I. Flik, B.I. Choi, A.C. Anderson, A.C. Westerheim, Thermal analysis and control for sputtering deposition of high-Tc superconducting films, J. Heat Transf. 114 (1992) 255–263, https://doi.org/10.1115/1.2911255.
[37] A. Segerstark, J. Andersson, L.-E. Svensson, Evaluation of a temperature measurement method developed for laser metal deposition, Sci. Technol. Weld. Join. 22 (2017) 1–6, https://doi.org/10.1080/13621718.2016.1169363.
[38] X. Xu, Perturbation of the substrate temperature by the impingement of laser ablated particles, J. Appl. Phys. 77 (1995) 6715–6717, https://doi.org/10.1063/1.359086.
[39] M. Kariniemi, J. Niinistö, T. Hatanpää, M. Kemell, T. Sajavaara, M. Ritala, M. Leskelä, Plasma-enhanced atomic layer deposition of silver thin films, Chem. Mater. 23 (2011) 2901–2907, https://doi.org/10.1021/cm200402j.
[40] D. Perednis, L.J. Gauckler, Thin film deposition using spray pyrolysis, J. Electroceram. 14 (2005) 103–111, https://doi.org/10.1007/s10832-005-0870-x.
[41] R.S.N. Kumar, A.V. Ramirez, P. Verding, P. Nivelle, F. Renner, J. D'Haen, W. Deferme, Deposition of ultra-thin coatings by a nature-inspired spray-on-screen technology, Commun. Eng. 2 (2023) 42, https://doi.org/10.1038/s44172-023-00093-0.
[42] A.S. Dinkar, H. Panchal, A review on thermal spray coating processes, 2 (2016).
[43] A.R. Govande, A. Chandak, B.R. Sunil, R. Dumpala, Carbide-based thermal spray coatings: a review on performance characteristics and post-treatment, Int. J. Refract. Met. Hard Mater 103 (2022) 105772, https://doi.org/10.1016/j.ijrmhm.2021.105772.